GSA Data Repository Item 2020067

Tasistro-Hart, A., Maloof, A., Schoene, B., and Eddy, M.P., 2020, Astronomically forced hydrology of the Late Cretaceous sub-tropical Potosí Basin, Bolivia: GSA Bulletin, https://doi.org/10.1130/B35189.1.

Data Repository

- Cross validation of the stratigraphic model
- Full grain by grain U-Pb CA-ID-TIMS isotopic data for the reported ages
- Measured section logs: IC1 MA2 MA3 MA4
- Magnetic susceptibility measurements
- Detailed discussion of any data preprocessing, including prewhitening of the time series and GPS data reduction.

U-Pb Zircon Geochronology Methods

Zircons were separated from potential volcanic samples using standard crushing techniques and density separation using a gold pan. Euhedral zircons with little to no rounding were then selected for analysis. Grains were not mounted and polished for cathodoluminescence imaging in order to preserve as much U and Pb for the analysis as possible. Photographs of the analyzed zircons are shown in Figure S1. The selected zircons were then analyzed by chemical abrasion-isotope dilution-thermal ionization mass spectrometry (CA-ID-TIMS) following methods modified from (Mattinson, 2005) and described in detail in (Samperton et al., 2015). All of the samples were spiked with the EARTHTIME $^{205}Pb^{233}U^{235}U$ (ET535) isotopic tracer (Condon, Schoene, McLean, Bowring, & Parrish, 2015) and analyzed on an IsotopX Phoenix TIMS at Princeton University. Mass dependent fractionation of Pb was corrected using an average $\alpha = 0.182 \pm 0.041$ (%/amu, 1SD abs.) $^{202}Pb^{205}Pb^{233}U^{235}U$ (ET2535) isotopic tracer (Condon et al., 2015) during 287 zircon analyses in the Princeton Geochronology Laboratory that used that tracer. Mass dependent fractionation of U was corrected using the known ration of $^{233}U/^{235}U$ in the ET535 isotopic tracer, and assuming a $^{238}U/^{235}U$ of 137.818 ± 0.0225 (Hiess, Condon, McLean, & Noble, 2012). Contamination from common Pb (Pb_c) was corrected using a Pb_c isotopic composition of $^{206}Pb/^{204}Pb = 18.17 \pm 0.38$ (1σ abs.), $^{207}Pb/^{204}Pb = 15.35 \pm 0.27$ (1σ abs.), $^{208}Pb/^{204}Pb = 37.35 \pm 0.77$ (1σ abs.) based on 53 procedural blanks run at Princeton University.

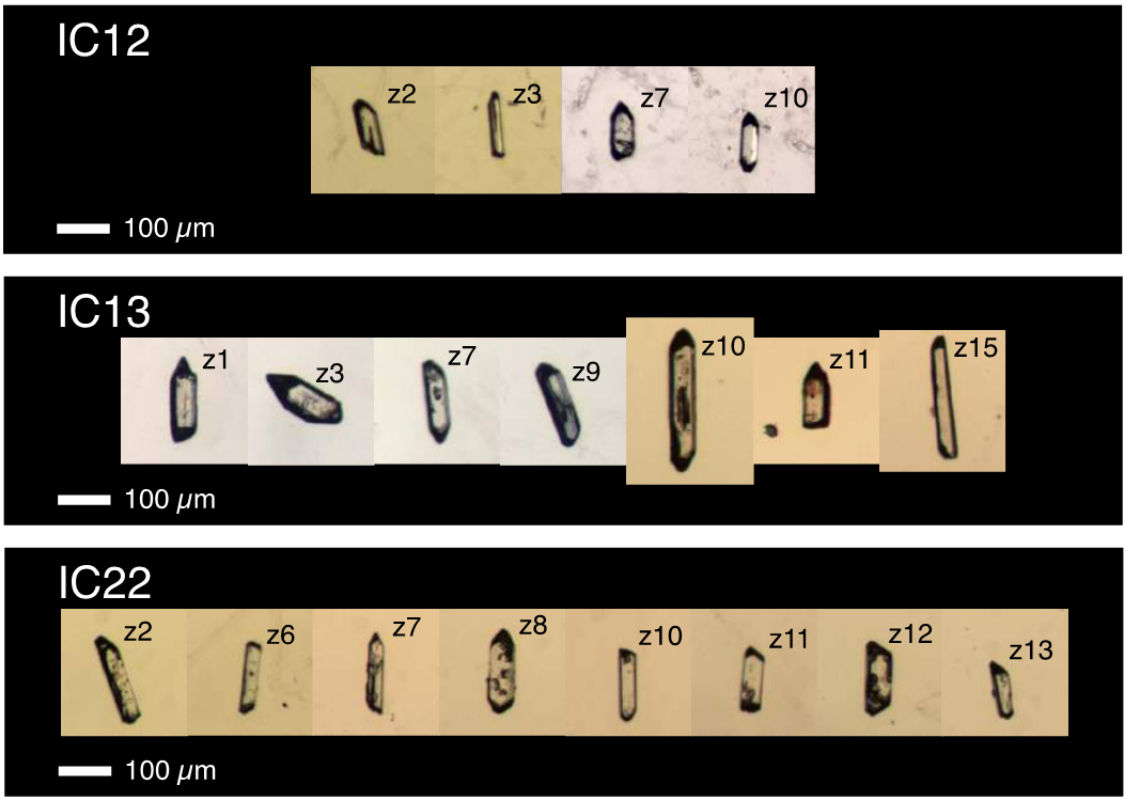

Figure S1 Photographs of the zircons analyzed from IC12, IC13, and IC22.

Thorium is preferentially excluded from zircon during crystallization and leads to initial secular disequilibrium in the ^{238}U -> ^{206}Pb decay chain. We correct for this disequilibrium using a constant ratio of Th and U partition coefficients ($f_{ThU}=D_{Th}/D_U$) between zircon and melt. We use a $f_{ThU}=0.33$ to calculate the $[Th/U]_{Magma}$ from which each zircon crystallized based on the experimental results for trace element partitioning between zircon and andesitic melt that are reported in (Rubatto & Hermann, 2007). For all $[Th/U]_{Magma}$ we apply an arbitrary uncertainty of ± 1 (2σ). Using a constant $[Th/U]_{Melt}$ of 2.8, consistent with the average [Th/U] in silicic tuffs (e.g Machlus et al. (2015)), does not appreciably change our results (Table S1).

The results of the U-Pb zircon geochronology are shown in concordia and rank order plots in Figure S2. The full isotopic data set is presented in "Compiled_UPb_Final.xls". Uncertainties are reported in the format ± A/B/C, where A is the analytical uncertainty, B includes uncertainty in the composition of the isotopic tracer, and C includes uncertainty related to the ^{238}U decay constant.

Table S1. Sensitivity of $^{206}Pb/^{238}U$ Zircon Dates to Th-Correction

Sample	Date Type	f_{ThU}=0.33	$[Th/U]_{Magma}$=2.8	Δt
IC12	Youngest Grain	70.20 ± 0.23 Ma[1]	70.13 ± 0.23 Ma[1]	0.070 Ma
IC13	Youngest Grain	68.87 ± 0.11 Ma[1]	68.897 ± 0.096 Ma[1]	0.027 Ma
IC13	Weighted Mean	68.944 ± 0.042 Ma[1]	68.952 ± 0.041 Ma[1]	0.008 Ma
IC22	Youngest Grain	72.01 ± 0.11 Ma[1]	72.02 ± 0.12 Ma[1]	0.010 Ma
IC22	Weighted Mean	72.089 ± 0.044 Ma[1]	72.100 ± 0.43 Ma[1]	0.011 Ma
MA 485.17	Youngest Grain	66.58 ± 0.22 Ma[1]	66.58 ± 0.22 Ma[1]	0.000 Ma

[1] Only analytical uncertainty is reported for this comparison.

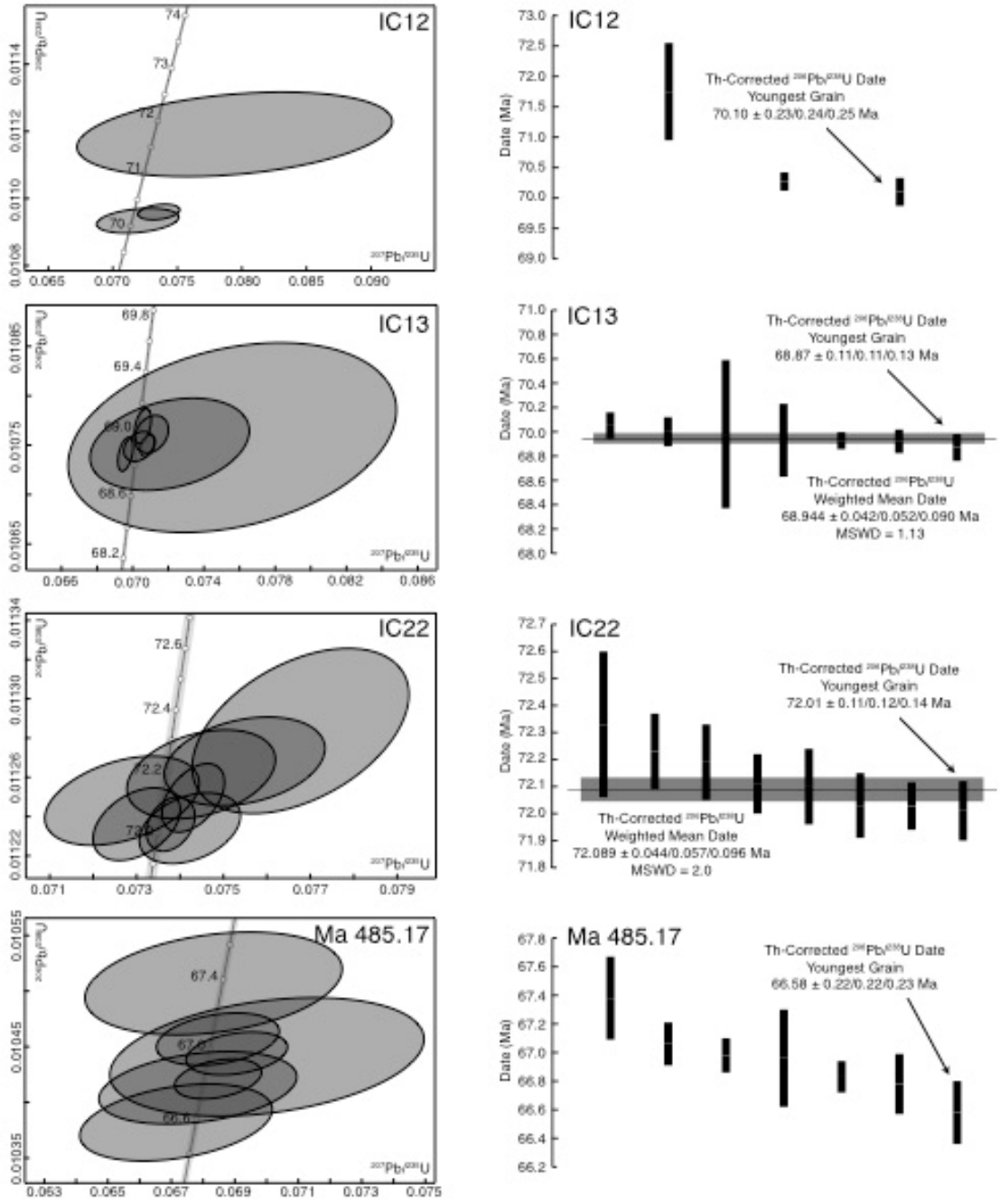

Figure S2. Concordia diagrams and rank order plots for the dated zircon in samples IC12, IC13, IC22, and MA 485.17. All dates are corrected for initial secular disequilibrium in the ^{238}U -> ^{206}Pb decay chain due to preferential exclusion of Th during zircon crystallization using a f_{ThU}=0.33 (see text for explanation). We report two date interpretations for samples with little age dispersion. The first is a weighted mean of all analyses and the second is the youngest grain only.

Trimble GPS Data

During the summer of 2016, at each of the sites we visited (Ichilula and Maragua), we set up a base station whose position was recorded by several thousand points collected by one of the Trimble rovers. These base station locations were corrected with data from BTRC and RDEO, nearby base stations maintained by the Instituto Geográfico Militar (IGM) of Bolivia. At all sites, each of the base station locations was known within reported uncertainties of less than 0.5 m.

Table S2: Locations of IGM base stations.

Station Name	Latitude	Longitude
BTRC	-19.1886	-64.9149
RDEO	-18.9016	-66.7681

At each site, the corrections of data taken with the Trimble rovers in the field by the local base station resulted in uncertainties typically less than 15 cm for each point. The breakdown by site as produced by the Trimble Pathfinder differential correction software is shown in Table S3.

Table S3: Reported precisions after correction of Trimble-collected points by base stations in the field.

Range of 1-std	Ichilula	Maragua
0-5 cm	23.58%	3.32%
5-15 cm	61.19%	80.62%
15-30 cm	0.72%	1.91%
30-50 cm	6.19%	6.79%
0.5-1 m	7.62%	5.87%
1-2 m	0.65%	1.25%
2-5 m	0.05%	0.24%
>5 m	0.00%	0.00%
total points	21267	46351

Point Cloud Classification at Maragua

Unlike at Ichilula, where the sparse vegetation roughly tracked beds and thus did not introduce significant noise into the spectral analysis, vegetation at Maragua did not discriminate and generally obstructed outcrop without regard for bedding. Thus, it was

necessary to classify and remove points corresponding to vegetation from the drone-derived point cloud.

We achieved this by training a linear support vector machine (SVM) with two classes: vegetation and outcrop. The vegetation training set contained 420,000 points, while the outcrop training set contained 1,660,000 points. The training areas are shown in Figure S3. 10,000 points were taken from each class as training data to train the linear SVM.

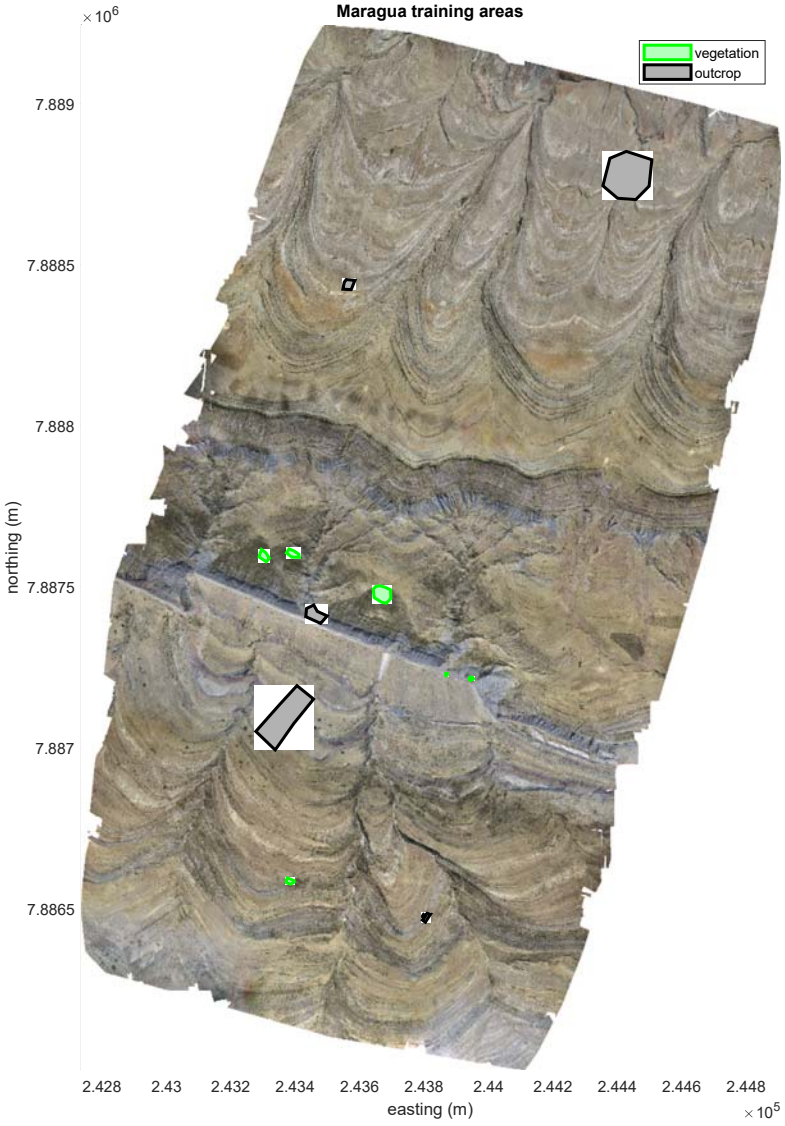

Figure S3. Areas for training the SVM used to classify outcrop and vegetation, totaling just over 2 million points (420,000 for vegetation, 1,660,000 for outcrop). 20,000 points (10,000 from each class) were used to train the SVM, the rest were used to test.

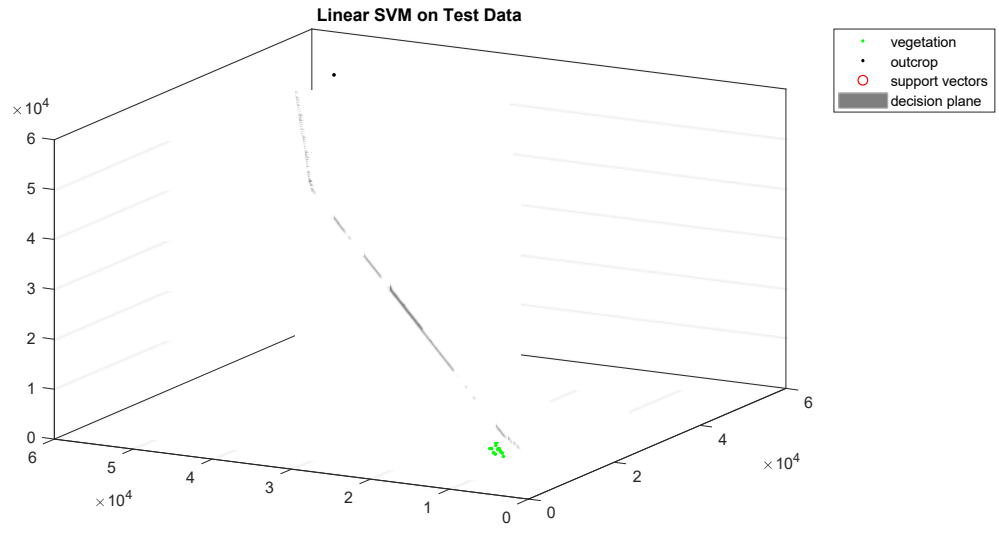

Figure S4. Linear SVM on the test data, achieving 98% classification accuracy.

The trained SVM is shown in Figure S4 along with the test data. The test sets were taken from the points not used to train the SVM, which amounted to just over 2 million points. The linear SVM was able to achieve 98% classification accuracy on the test data, which was sufficient for our needs and comparable to the results of SVMs utilizing other kernels, for instance the Gaussian kernel.

Stratigraphic Potential Model

Empirical Covariance Functions

Figure S5 shows the gradient components of measured strikes and dips at Ichilula. Rough axes of anisotropy are also shown, with the minor axis defined to be running parallel to strike and the major axis perpendicular. These axes were the natural choice at Ichilula, where bedding changed most in the direction of dip, towards the axis of the

syncline. Drifts in each component of the gradient are evident from map view, and Figure S6 shows these drifts projected onto the major and minor axes of anisotropy.

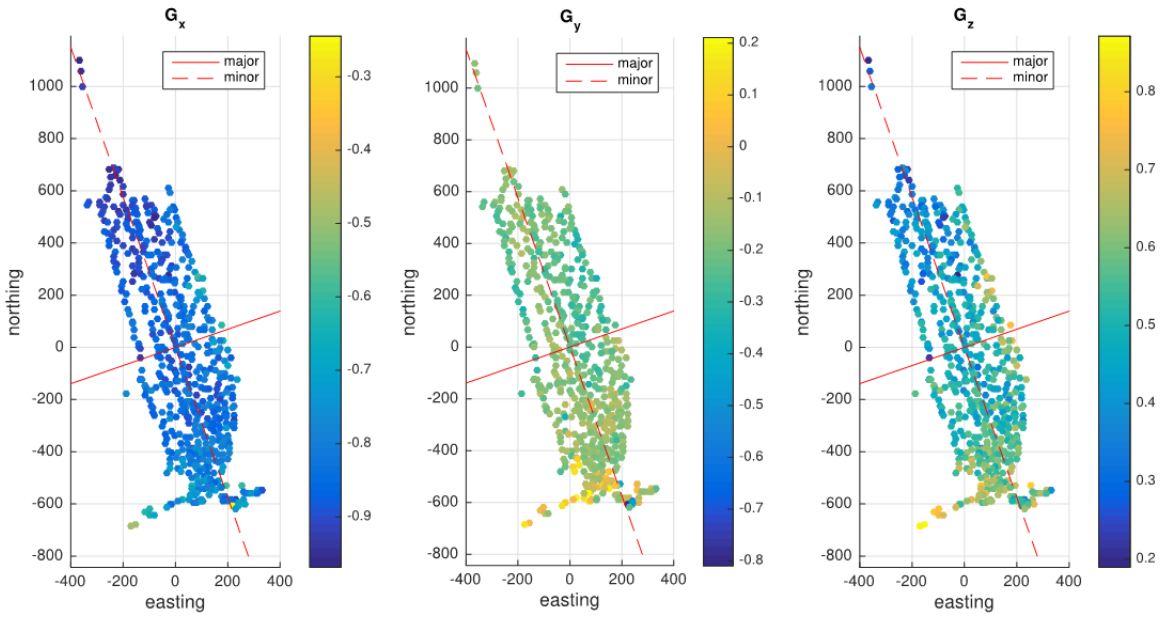

Figure S5. Components of the gradient in x,y,z coordinate directions shown in map view. Major and minor axes of anisotropy in the covariance are overlain, with the minor axis tracing the along-strike direction of the strata

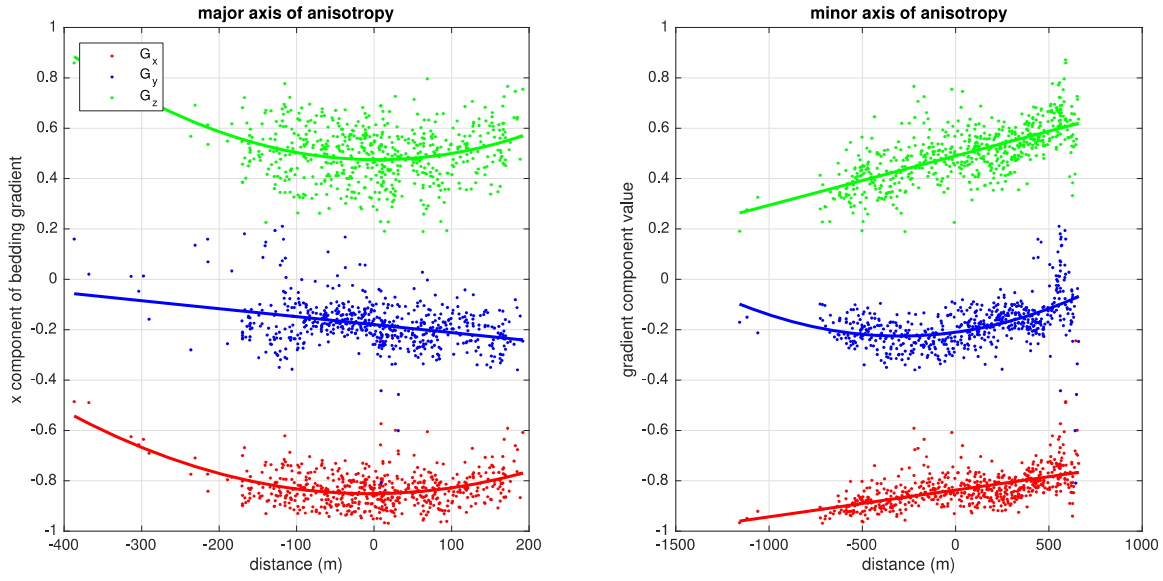

Figure S6. Drifts in the x,y,z components of the gradient along the major and minor axes of anisotropy, demonstrating larger scale structures that should not be considered as part of the statistical description of the gradient data.

It is necessary to account for the drifts prior to estimating the covariance parameters, since the drifts represent systematic changes in the mean of the random variable that we are trying to interpolate. Removing drifts with second order polynomial surfaces is necessary to produce a stationary spatial series of gradient data.

Figure S7 shows the variograms for each component of the gradient without accounting for drift, illustrating the parabolic behavior of the empirical variogram along the major axis of anisotropy for each gradient component. Variograms should exhibit concave profiles, so parabolic behavior is indicative of drift that needs to be accounted for.

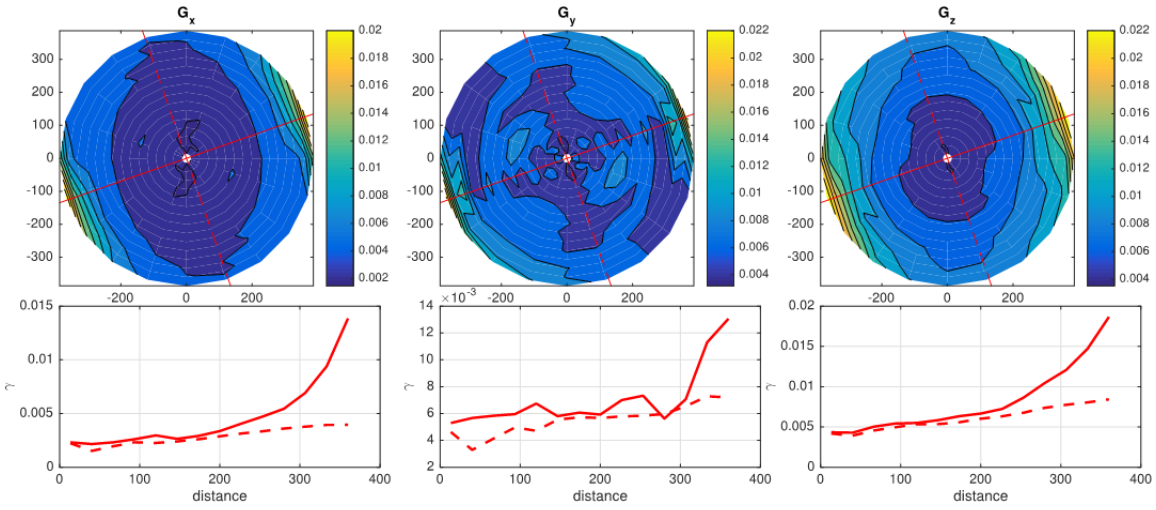

Figure S7. Variograms for each component of the gradient data showing 2-D anisotropy in the top row and 1-D profiles along the major and minor axes of anisotropy in the bottom row. Parabolic behavior along the major axis indicates the presence of drift, which should be removed.

Figure S8 demonstrates the impact of removing drift on the empirical variograms of the same data. The overall anisotropy of the gradient data has diminished, and the empirical variograms are no longer parabolic. The operational range of 600~m and sill of 0.002 for the isotropic case are taken from drift-corrected gradient data at Ichilula,

generally falling in between the empirical variograms along the major and minor axes of anisotropy shown in Figure S8.

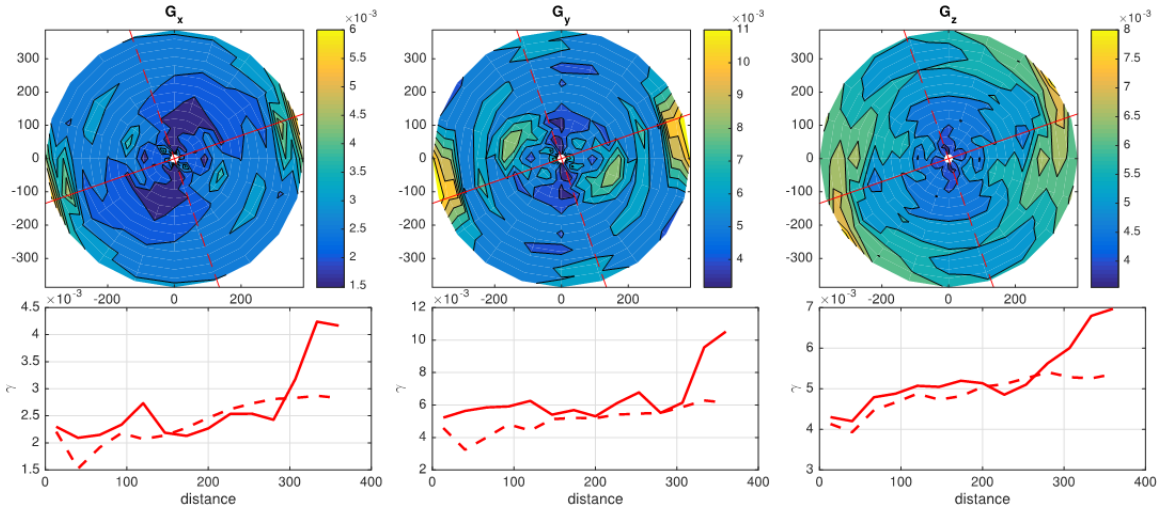

Figure S8. Same as Figure S7 except that the gradient data in this case were corrected for drifts by subtracting a fitted quadratic surface. The 1-D profiles along the major and minor axes of anisotropy are now closer, and the parabolic behavior of the variogram from Figure S7 data has disappeared.

Covariance Model Cross-Validation

We also considered how the choices of range and sill affected the interpolated potential along the bed traces. The model is completely unresponsive to the choice of sill in the isotropic case, since the magnitude of covariance is irrelevant for assigning weights to observations when covariance is identical in every direction. At Ichilula, isotropic covariance of potential is not strictly realistic, since sedimentary bedding in the absence of complex structural features imposes a constant strike and dip that determines axes of anisotropy. At Ichilula, these axes run roughly north-south (strike) east-west (dip), so one would expect potential values to covary more strongly with a north-south orientation because stratigraphic height remains constant along strike. By utilizing an isotropic model and appropriately accounting for larger structures via a drift function, however, we

have demonstrated that knowledge of the axes of anisotropy is not absolutely necessary to accurately model the stratigraphy.

The model is, however, sensitive to the choice of range. Figure S9 shows the potentials corresponding to the bed traces at Ichilula, relative to a covariance model with a range of 450 m, for ranges from 100 m to 1000 m. For all but the smallest range of 100 m, the offset in interpolated potential along bed traces was constant, meaning that, beyond an initial offset in potential between the first and second bed traces, the potential increments were identical for all ranges. Thus, there is not an unpredictable stretching of potential values for different ranges, meaning that the choice of range does not detrimentally impact the mapping between potential and time. Even for a small range of 100 m, the difference in interpolated potential varied only slightly. The offset in potential between the first and second bed traces also approaches zero for models with larger ranges, indicating a more stable solution that is essentially already achieved by a range of 600 m. This offset is due to the undersampling and imprecision of our sampling of the first bed trace, which was the contact between the Chaunaca and the Lower El Molino at Ichilula. We found the contact convincingly in only a dozen locations, and the next nearest bed trace is quite some distance from the contact because we chose to ignore the ~80 m of transgressive sandstones of the bottom Lower El Molino when mapping bed traces. Thus, 600 m was a reasonable range for Ichilula.

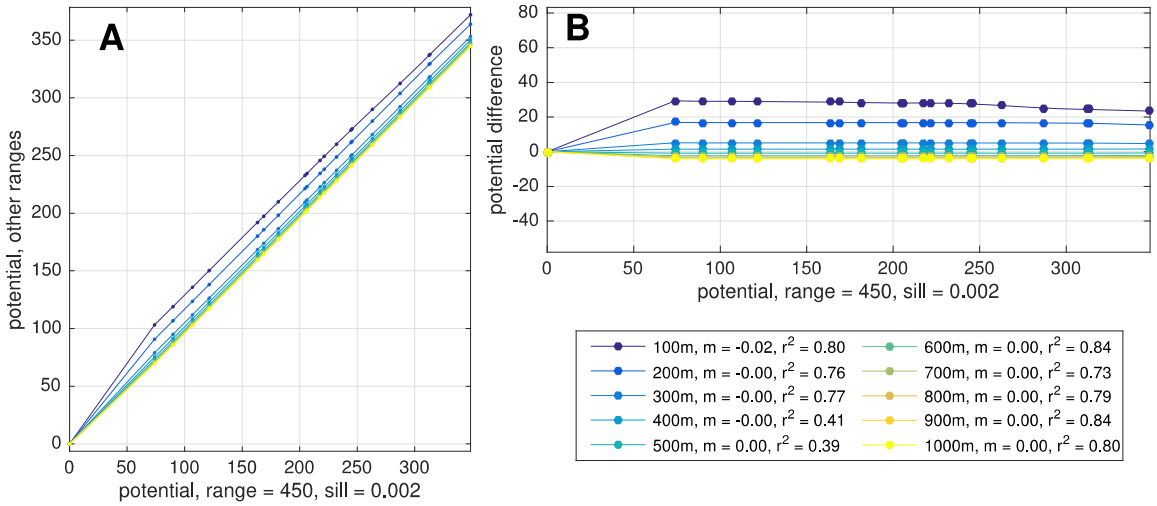

Figure S9. (A) Interpolated potentials at Ichilula such that the first bed trace always has zero potential plotted against the potentials the same traces attained from a model with a range of 450 m and a sill of 0.002. (B) The difference in potential at each bed trace between the model with a range of 450 m and models with ranges from 100 m to 1000 m. The change between traces is constant (ignoring the first trace) for all ranges except 100 m. For ranges above 500 m, the offset is constant and all the ranges have the same effect on the interpolated potentials at the bed traces.}

A similar approach was taken for the covariance model at Maragua. Table S4 shows the parameters used in the covariance models for both Ichilula and Maragua.

Table S4. Covariance model parameters

	Ichilula	Maragua
Sill	0.002	0.005
Range	600 m	1000 m

Bed Trace Sensitivity Tests

We cross-validated the potential model by checking how closely the model was able to recreate interpolated potentials along bed traces by iteratively removing a bed trace from the model and then computing potentials along all bed traces, including the one that was no longer in the model. The figures in the folder "Ichilula_bedtrace_xval" show the results of this cross-validation at Ichilula. Each figure corresponds to the bed trace that was left out of the model during the cross-validation. Each histogram shows the

interpolated potential values at points along the bed trace. The thick black line shows the potential for that bed when all bed traces are included in the model. The other lines correspond to the potential values along the bed trace when it is included in the model, but when one of the other traces is not. Ideally, the histogram would be centered on the thick black line, and there would not be significant spread between the other lines, since we would hope that each trace would achieve roughly the same potential (given a constant origin) despite a lack of complete data. For many of the traces, this pattern is what emerges, especially for traces not at the top or bottom of the stratigraphy. In each analysis, the potential values were very sensitive to the presence of traces at the bottom of the stratigraphy, i.e. traces 4, 12, and 18.

This sensitivity is understandable through the availability of gradient information: moving westwards, dip increases, so the under-representation of shallower dips in the east causes the model to increase potential more quickly in the absence of bed traces, which would otherwise constrain the potential. Thus, when traces 4 or 12 are absent, this is the reason for the overestimation of potential at all other beds. Interestingly, when trace 18 is absent, it actually results in the opposite, causing potential to be consistently less than when the trace is included in the model. Trace 18 is notably the first long trace of high quality. Trace 12 followed a contact with poor exposure tracing the transition from the last transgressive sandstone to the first shales of the carbonate-rich portion of the El Molino. Trace 4 is also poorly defined and follows the exceedingly rare Chaunaca-El Molino contact. Trace 18, on the other hand, follows a thick ribbonite unit, the first carbonate of the section. These factors do not explain the behavior of the potential model

when trace 18 is removed, but they do underpin its importance to the model as the stratigraphically lowest trace of high quality.

Detection of Faulty Bed Trace in IC1

Figure S10B shows the difference between interpolated stratigraphic potential and measured stratigraphic height along the section IC1 at Ichilula. An abrupt break at around 110 m in the otherwise smoothly varying curve indicated either the presence of a fault or a mistaken bed trace. This point in the measured stratigraphy corresponds exactly to the first trace, where we cross the south side of the gully visible in Figure 1A to the north side of the gully in order to avoid structural complexity awaiting further up-section. We corrected for the trace by adding 4.5 m to stratigraphic heights taken after the trace, which made the curve in Figure S10B smoothly varying.

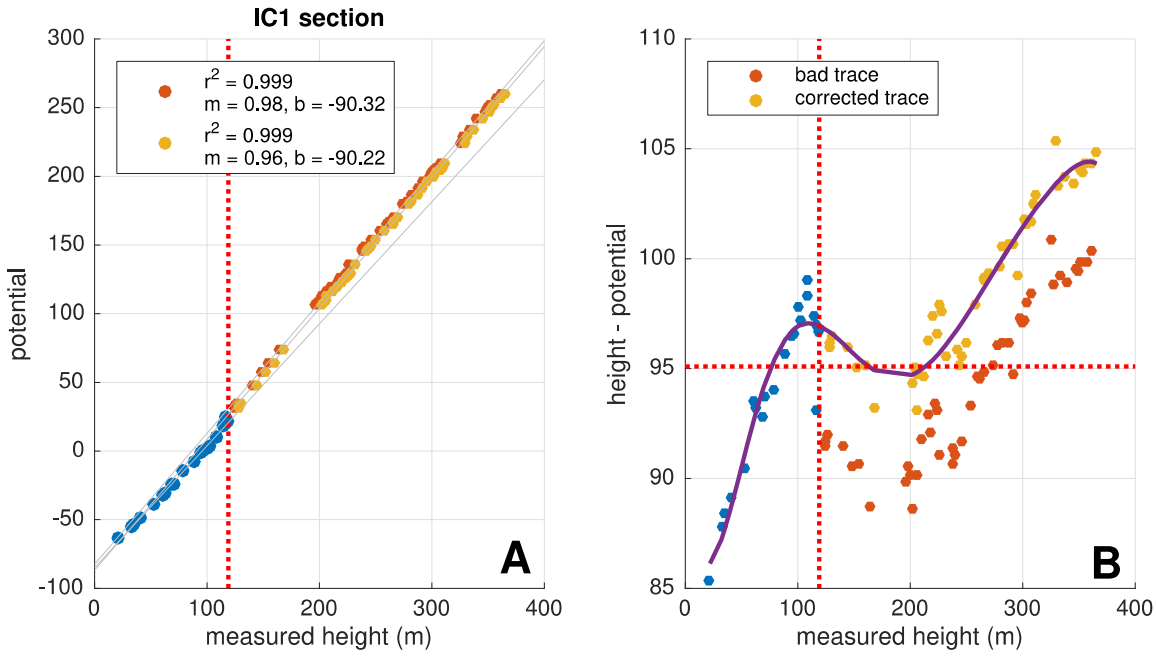

Figure S10. (A) Plot of measured height against interpolated potential at Ichilula, as in Figure 1C. The vertical dashed line shows the height chosen as the origin value for the potential model. (B) Difference between measured stratigraphic height and interpolated potential, where orange points show points revealing the faulty bed trace and yellow points show the ~4.5 m correction to stratigraphic heights.

Gradient Cross-Validation

We also performed cross-validation on the gradient data. In addition to interpolating potential at any point, the stratigraphic model allows for interpolation of the gradient of potential at any point. We cross-validated the gradient data at both sites by in turn removing each strike and dip observation and interpolating the strike and dip at the location of the ignored observation. We then computed the angle between the interpolated and actual gradient. The histogram of these angles is shown for Ichilula in Figure S11. Of the 558 measurements, 91% of the interpolated strikes and dips are less than 10º, and all are less than 20º away from the measured strikes and dips. We found this result to be acceptable given that we anticipated uncertainties in strikes and dips on the order of 5-10º.

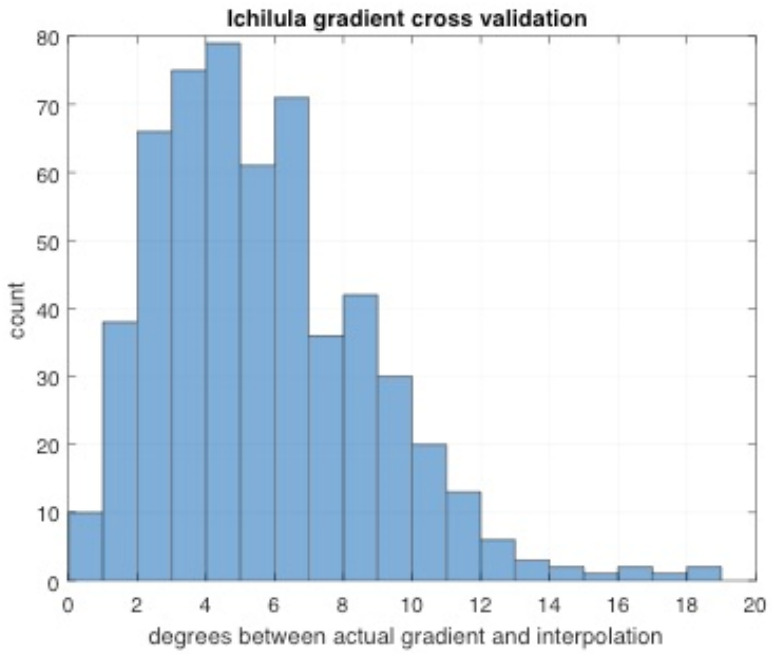

Figure S11. Gradient cross-validation for Ichilula showing the distribution of angles between observed gradient data and interpolated data.

The results for gradient cross-validation at Maragua are similar, as shown in Figure S12. At Maragua, 95% of interpolated gradients were within 10º of the measured gradient. The tail of the distribution of degree misfits was a bit longer at Maragua, with a handful of gradients interpolating 20º or more away from the measured gradient. Overall, however, we are satisfied with the model's ability to recreate our measurements, given the a priori 5-10º measurement uncertainty that we assumed for strikes and dips.

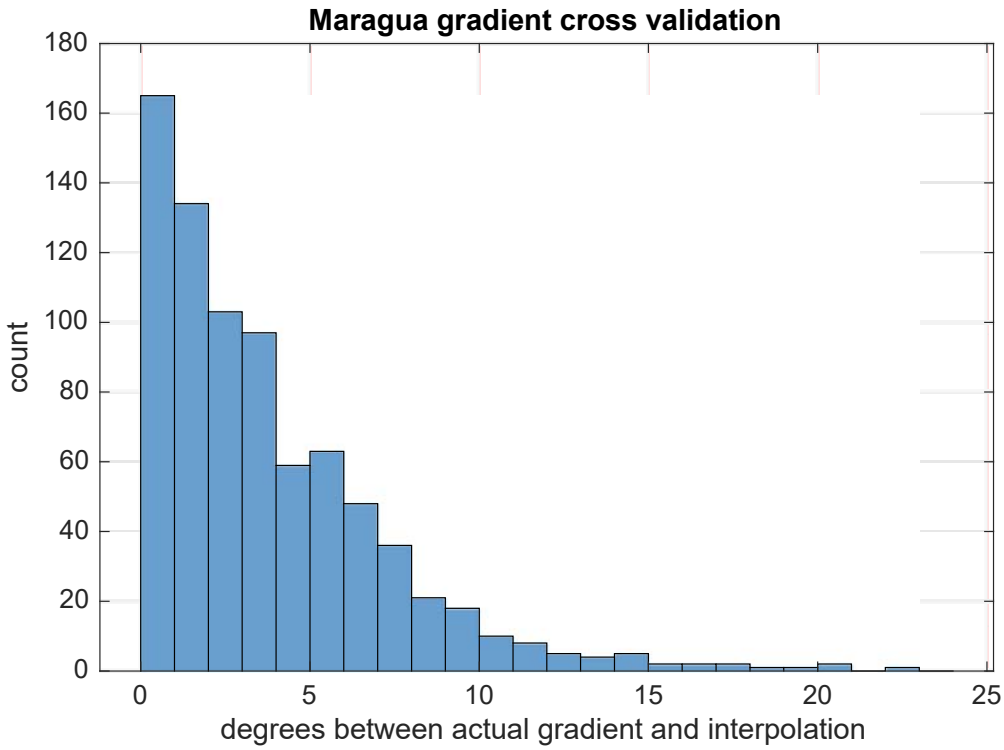

Figure S12. Gradient cross-validation for Ichilula showing the distribution of angles between observed gradient data and interpolated data

Sensitivity of Spectral Analysis to IC12 at Ichilula

The transitional behavior of the Lower El Molino from precession to obliquity-dominated sedimentation around 70.4 Ma could be attributed, at least at Ichilula, to the inclusion of IC12 in the age model. The age of IC12 corresponds roughly to that of the transition, so the slight deviation from constant sedimentation introduced by

incorporating this sample could have rearranged spectral power to give the impression this transition. However, removing IC12 from the age model did not affect the emergence of obliquity in the top Lower El Molino (Figures S13 & S14), and the presence of the same transition at Maragua indicates that it is a robust feature and a significant change in the basin's sensitivity to orbital forcing.

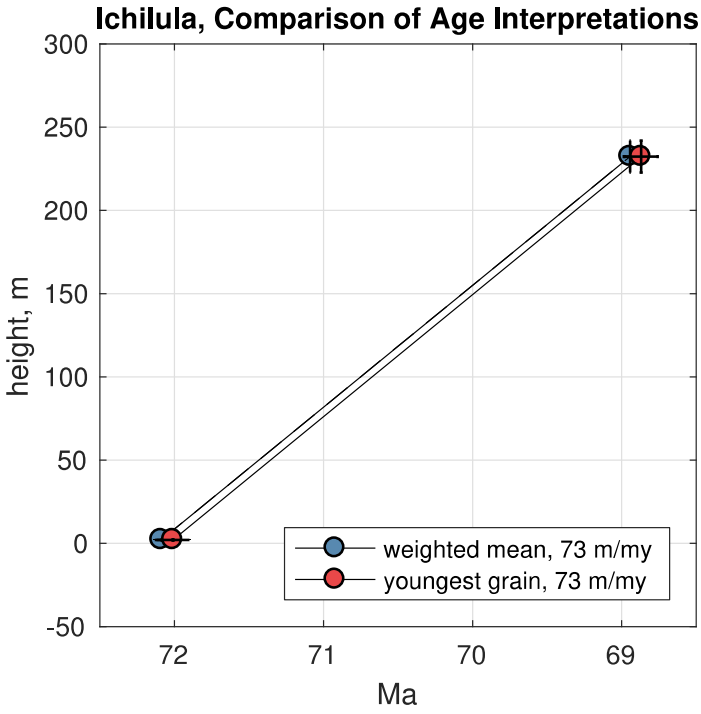

Figure S13. Comparison of age models resulting from weighted mean versus youngest grain ages of IC13 and IC22. The youngest grain ages, as anticipated, shift the sedimentation curve towards younger ages, but the average slope remains 73 m my^{-1}.

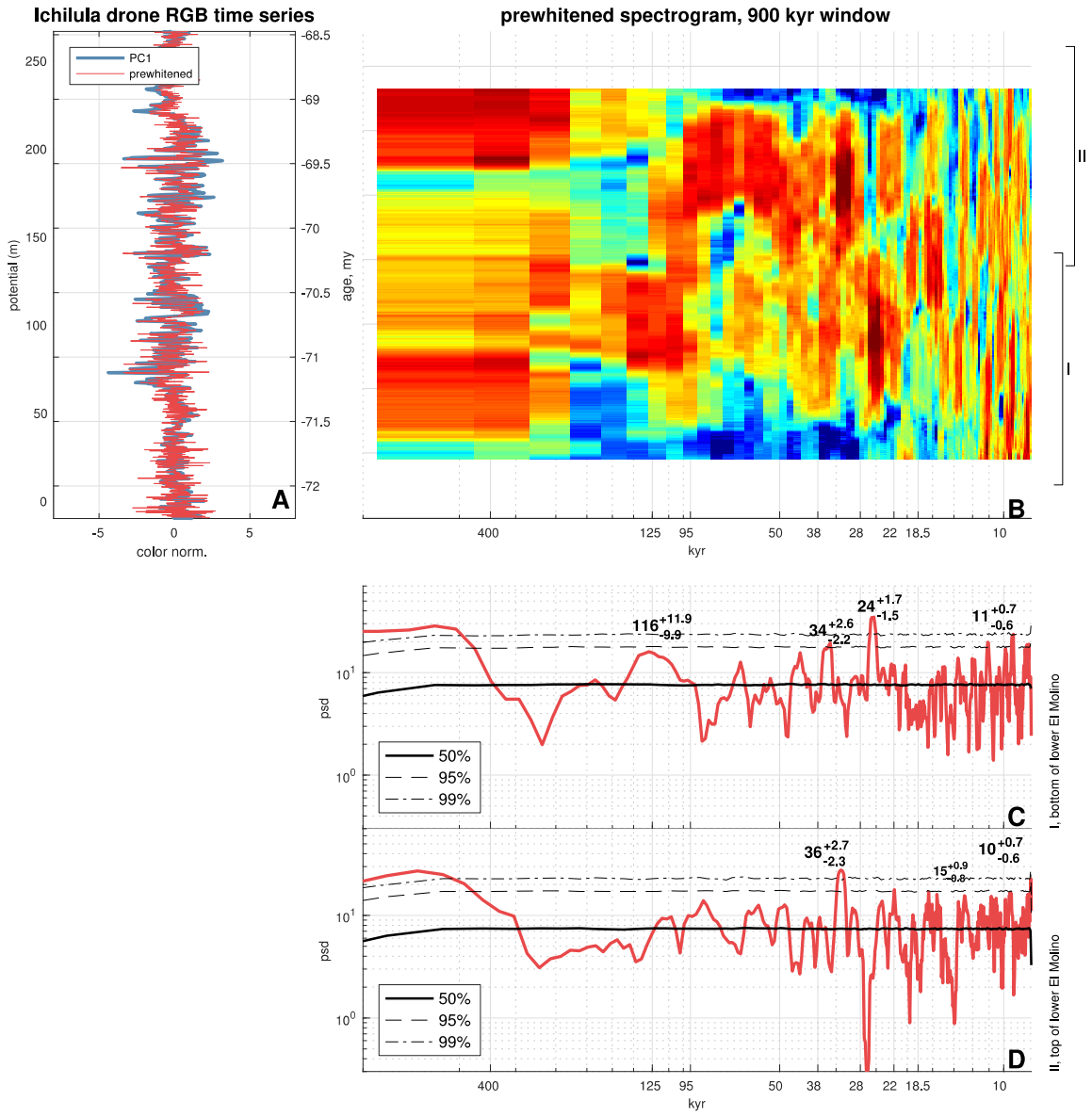

Figure S14. Same as Figure 5 but without including IC12 in the age model.

Orbital Periods during Late Cretaceous

Figure S15 shows the orbital solutions of J. Laskar et al. (2004) during the period 73-64 Ma for each orbital forcing. During deposition of the El Molino, these results indicate that the periods of obliquity and precession are slightly shorter than their present values. The periodicities of eccentricity have not changed substantially, and the

periodicities of eccentricity shown in Figure S15 do not vary substantially between any of the simulations a-d of Jacques Laskar (2011) during the same time interval.

Figure S16 shows the variability in summer insolation for the paleolatitudes of the Western Interior, Songliao, Basque, and Potosí Basins, computed using the orbital solutions of Jacques Laskar (2011). All paleolatitudes were computed by the paleolatitude calculator (van Hinsbergen et al., 2015). For all basins, orbital variability in summer insolation is dominated by precession, with some variation at a periodicity of 28 kyr that is also due to precession.

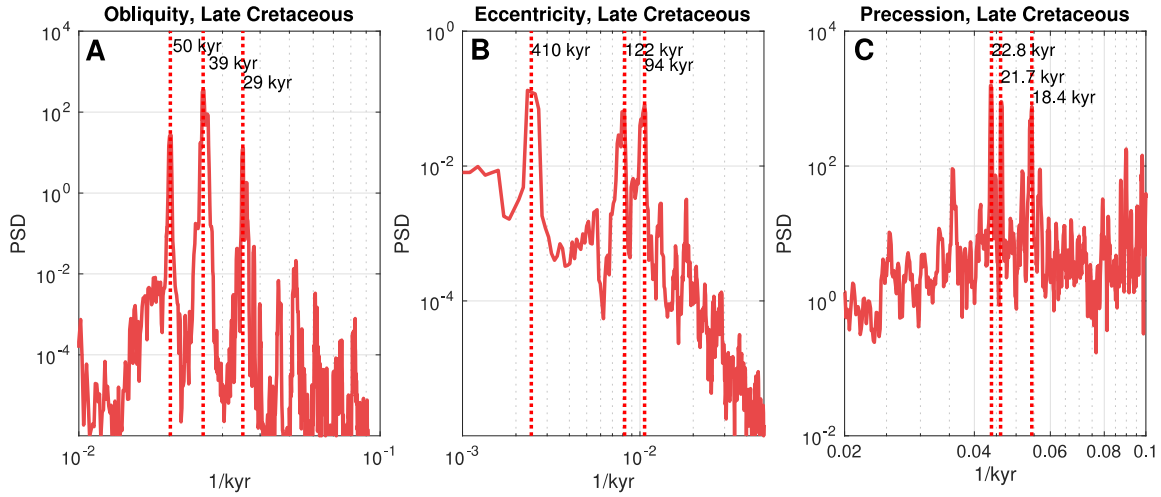

Figure S15. Power spectral density estimate for the solutions of (A) obliquity, (B) eccentricity (C) precession from J. Laskar et al. (2004) during the Late Cretaceous, 73-65 Ma. The peaks for obliquity and precession are all at higher frequencies than the present due to the smaller Earth-Moon distance in the geologic past (Berger, Loutre, & Laskar, 1992).

As expected, the sensitivity in summer insolation variability to obliquity depends on the paleolatitude of the basin, with the more northern Western Interior and Songliao Basins exhibiting significantly higher sensitivity to obliquity. This insolation sensitivity, in the presence of a straightforward linear insolation-hydrology response, could explain the presence of obliquity in the proxies reported from these basins by Locklair and

Sageman (2008); Wu et al. (2014). The Potosí and Basque Basins, however, the obliquity sensitivity of summer insolation is two orders of magnitude less than the sensitivity to precession, making the brief appearance of obliquity-scale variability in the RGB and MS series from the Potosí Basin difficult to explain on the basis of local forcing.

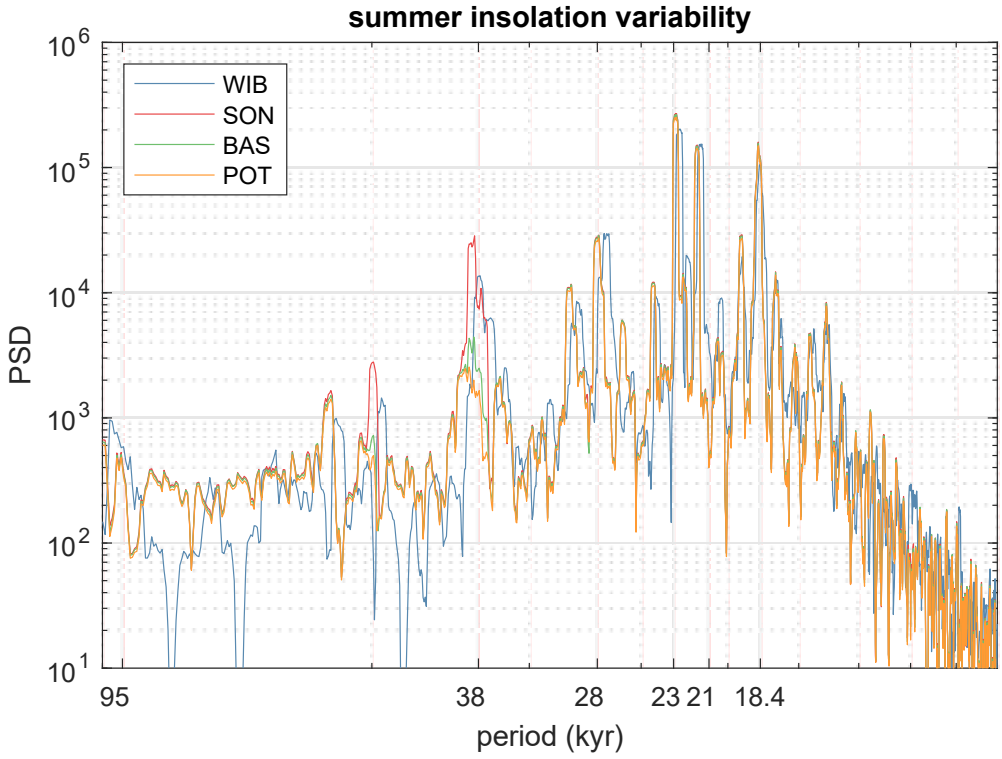

Figure S16. Power spectral density estimates of summer insolation variability for the Western Interior (WIB), Songliao (SON), Basque (BAS), and Potosí (POT) Basins.

Magnetic Susceptibility Measurements

Figure S17 shows the distribution in relative magnitudes of measurements of MS from both Ichilula and Maragua relative to the uncertainties in those measurements, demonstrating that the level of uncertainty is less than the variability in the measurement values. Thus, periodicities present in the MS series should not be overwhelmed by measurement uncertainty.

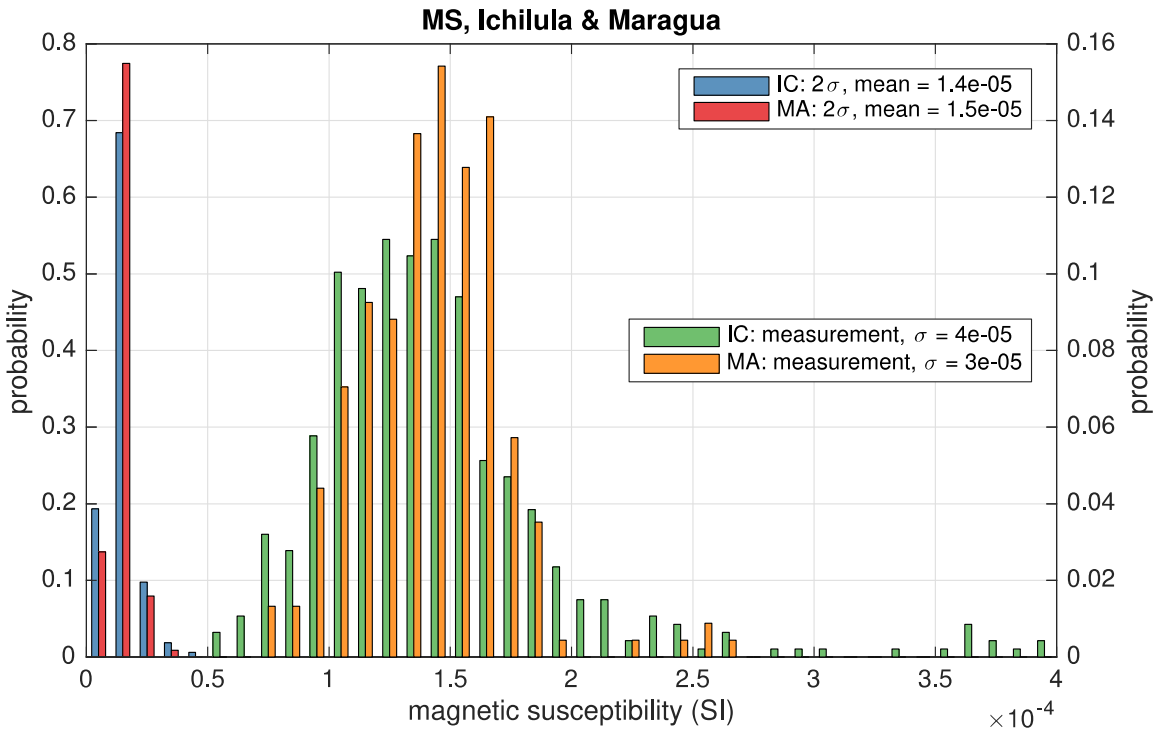

Figure S17. Distribution of measurements of magnetic susceptibility for samples at Ichilula and Maragua. These values are measurement means after at least 10 individual measurements of a sample. The red and blue bars show the distribution of 2σ variability after at least 10 individual sample measurements for the same samples. The average 2σ measurement uncertainty is several times less than the variability amongst measurements themselves. The reported standard deviation of the average measurements ignores values above 0.3×10^{-3} SI and refers to the width of the measurement histograms, not variability within one sample.

REFERENCES CITED

Berger, A., Loutre, M. F., & Laskar, J. (1992). Stability of the astronomical frequencies over the Earth's history for paleoclimate studies. *Science, 255*, 560-566. doi:https://doi.org/10.1126/science.255.5044.560

Condon, D. J., Schoene, B., McLean, N. M., Bowring, S. A., & Parrish, R. R. (2015). Metrology and traceability of U–Pb isotope dilution geochronology (EARTHTIME Tracer Calibration Part I). *Geochimica et Cosmochimica Acta, 164*, 464-480. doi:https://doi.org/10.1016/j.gca.2015.05.026

Hiess, J., Condon, D. J., McLean, N., & Noble, S. R. (2012). $^{238}U/^{235}U$ systematics in terrestrial Uranium-bearing minerals. *335*(6076), 1610-1614. doi:https://doi.org/10.1126/science.1215507

Laskar, J. (2011). The limits of Earth orbital calculations for geological time-scale use. *Astronomy and Astrophysics, 532*, 1-15. doi:https://doi.org/10.1098/rsta.1999.0399

Laskar, J., Robutel, P., Joutel, F., Gastineau, M., Correia, A. C. M., & Levrard, B. (2004). A long-term numerical solution for the insolation quantities of the Earth. *Astronomy and Astrophysics, 428*, 261-285. doi:https://doi.org/10.1051/0004-6361:20041335

Locklair, R. E., & Sageman, B. B. (2008). Cyclostratigraphy of the Upper Cretaceous Niobrara Formation, Western Interior, USA: A Coniacian-Santonian orbital timescale. *Earth and Planetary Science Letters, 269*, 540-553. doi:https://doi.org/10.1016/j.epsl.2008.03.021

Machlus, M. L., Ramezani, J., Bowring, S. A., Hemming, S. R., Tsukui, K., & Clyde, W. C. (2015). A strategy for cross-calibrating U-Pb chronology and astrochronology of sedimentary sequences: An example from the Green River Formation, Wyoming, USA. *Earth and Planetary Science Letters, 413*, 70-78. doi:https://doi.org/10.1016/j.epsl.2014.12.009

Mattinson, J. M. (2005). Zircon U-Pb chemical abrasion ("CA-TIMS") method: Combined annealing and multi-step partial dissolution analysis for improved precision and accuracy of zircon ages. *Chemical Geology, 220*, 47-66. doi:https://doi.org/10.1016/j.chemgeo.2005.03.011

Rubatto, D., & Hermann, J. (2007). Experimental zircon/melt and zircon/garnet trace element partitioning and implications for the geochronology of crustal rocks. *Chemical Geology, 241*(1), 38-61. doi:https://doi.org/10.1016/j.chemgeo.2007.01.027

Samperton, K. M., Schoene, B., Cottle, J. M., Keller, C. B., Crowley, J. L., & Schmitz, M. D. (2015). Magma emplacement, differentiation and cooling in the middle crust: Integrated zircon geochronological–geochemical constraints from the Bergell Intrusion, Central Alps. *Chemical Geology, 417*(Supplement C), 322-340. doi:https://doi.org/10.1016/j.chemgeo.2015.10.024

van Hinsbergen, D. J. J., de Groot, L. V., van Schaik, S. J., Spakman, W., Bijl, P. K., Sluijs, A., . . . Brinkhuis, H. (2015). A paleolatitude calculator for paleoclimate studies. *PLOS ONE, 10*(6), e0126946. doi:https://doi.org/10.1371/journal.pone.0126946

Wu, H., Zhang, S., Hinnov, L. A., Jiang, G., Yang, T., Li, H., . . . Wang, C. (2014). Cyclostratigraphy and orbital tuning of the terrestrial upper Santonian–Lower Danian in Songliao Basin, northeastern China. *Earth and Planetary Science Letters, 407*, 82-95. doi:https://doi.org/10.1016/j.epsl.2014.09.038